PCCP

PAPER

Cite this: *Phys. Chem. Chem. Phys.*, 2017, **19**, 1425

Partial oxidation of the absorber layer reduces charge carrier recombination in antimony sulfide solar cells†

Karl C. Gödel,[a] Bart Roose,[b] Aditya Sadhanala,[a] Yana Vaynzof,[cd] Sandeep K. Pathak[e] and Ullrich Steiner*[b]

Received 4th November 2016,
Accepted 6th December 2016

DOI: 10.1039/c6cp07559b

www.rsc.org/pccp

We investigate the effect of a post heat treatment of the absorber layer in air for antimony sulfide (Sb_2S_3) sensitized solar cells. Phenomenologically, exposing the Sb_2S_3 surface of sensitised solar cells to air at elevated temperatures is known to improve device performance. Here, we have investigated the detailed origins of this improvement. To this end, samples were annealed in air for different time periods and the build-up of an antimony oxide layer was monitored by XPS. A very short heat treatment resulted in an increase in power conversion efficiency from η = 1.4% to η = 2.4%, while longer annealing decreased the device performance. This improvement was linked to a reduction in charge carrier recombination at the interface of Sb_2S_3 with the organic hole conductor, arising from the oxide barrier layer, as demonstrated by intensity modulated photovoltage spectroscopy (IMVS).

Introduction

Solar cells possess significant potential in becoming a substantial energy source in the future. Several properties are crucial for photovoltaic devices to substitute non-renewable energy production, such as a high power-conversion efficiency, long-term stability and low production costs. Dye-Sensitised solar cells (DSSCs) were proposed as a cheap and easily processable alternative to conventional photovoltaic cells.[1] The possible leakage of liquid electrolytes and the degradation of the organic light absorber in DSSCs lead however to low device stabilities.[2] Solid-state sensitized solar cells with inorganic absorbing materials can overcome these problems. Due to its high absorption coefficient ($\alpha \approx 1.8 \times 10^5$ cm^{-1} at λ = 450 nm), long-term stability and suitable direct band-gap of $E_g \approx 1.7$ eV, crystalline Sb_2S_3 (stibnite) is a promising light absorber for solid-state sensitized solar cells.[3–6] Power-conversion efficiencies of up to η = 7.5% have been achieved using this material.[7] The architecture of these devices consists of a transparent electrode, such as fluorine-doped tin-oxide, a thin blocking layer of crystalline TiO_2 (titania) and a mesoporous TiO_2 layer for electron conduction. This porous film of titania nano-crystals provides a high surface area, which is covered by a thin layer of antimony sulfide as an absorber material. For the hole transport, different inorganic and organic hole conducting materials, such as copper thiocyanate (CuSCN), 2,2′,7,7′-tetrakis-(*N*,*N*-di-4-methoxyphenylamino)-9,9′-spirobifluorene (spiro-OMeTAD) and the conducting polymers poly[2,6-(4,4-bis-(2-ethylhexyl)-4*H*-cyclopenta [2,1-*b*;3,4-*b*]dithiophene)-*alt*-4,7(2,1,3-benzothiadiazole)] (PCPDTBT) and poly(3-hexylthiophene) (P3HT), were investigated.[4,5,8,9] The organic hole transport materials (HTMs) typically exhibit better device performance because of the efficient thiol bonding to Sb_2S_3.[5] The antimony sulfide deposition itself can be conducted in aqueous and non-aqueous chemical baths at low temperatures (<10 °C).[6,10–12] Both methods yield amorphous Sb_2S_3 films, which have to be annealed at 250–300 °C in an oxygen-free atmosphere.

Several publications reported improved performance in devices containing antimony sulfide active layers that were allowed to cool in air after annealing.[4,8,9,14–17] This leads to the hypothesis that the formation of a thin antimony oxide film may reduce charger carrier recombination in these devices. Our goal is here to understand this effect and optimise it. This study carries out a detailed investigation of Sb_2S_3 oxidation and links it to the performance of photovoltaic devices. The change of the material properties during heating in air was studied by X-ray photoelectron spectroscopy (XPS), X-ray diffraction (XRD) and UV-vis spectroscopy. The variation in device efficiency was tested by standard photovoltaic measurements. In addition, the electron

[a] *Cavendish Laboratory, Department of Physics, University of Cambridge, UK*
[b] *Adolphe Merkle Institute, Rue des Verdiers, Fribourg, Switzerland. E-mail: ullrich.steiner@unifr.ch*
[c] *Kirchhoff Institute for Physics, Heidelberg University, Im Neuenheimer Feld 227, Germany*
[d] *Centre for Advanced Materials, Heidelberg University, Im Neuenheimer Feld 225, Germany*
[e] *Centre for Energy Studies, Indian Institute of Technology, Delhi, India*

† Electronic supplementary information (ESI) available. See DOI: 10.1039/c6cp07559b

transport and recombination behaviour was studied by intensity modulated photocurrent and photovoltage spectroscopy (IMPS and IMVS, respectively).

Characterisation of annealed antimony sulfide

To probe whether the band-gap of the material changes upon heating in air, annealed samples were characterised by absorption spectroscopy. Fig. 1a shows UV-vis measurements of a single flat antimony sulfide sample obtained using a heating stage with a transmittance path. The change of the absorption spectrum was monitored *in situ* for 25 min in steps of 30 seconds during annealing at 200 °C in air. The complete set of recorded spectra is shown as a 2D map in the ESI† (Fig. S2). The measurement traces are nearly identical for oxidation times up to 25 min. When kept at 200 °C for 15 h, however, the sample colour changed from dark brown to pale white, indicating a dramatic change in the absorption spectrum (Fig. S3, ESI†). This demonstrates that 200 °C is high enough to oxidise the sample. Note that absorption spectroscopy measures the bulk properties of the material and is not sensitive to thin surface layers.

One possible cause for the previously reported efficiency improvement of annealed Sb_2S_3 solar cells could arise from a reduction in the density of inter bandgap states, also called trap states. These can be probed by the extremely sensitive absorption photothermal deflection spectroscopy (PDS).[18,19] Fig. 1b shows the normalised PDS absorbance of annealed antimony sulfide films on mesoporous TiO_2 in a semi-logarithmic plot. Inter bandgap states give rise to light absorption at energies below the band gap. The relevant energy region for the monitoring of these states therefore lies below the band gap of antimony sulfide of E_g = 1.7 eV. The absorbance variation in the 1–1.5 eV region lies within the experimental error and therefore does not support the hypothesis that a reduction in the density of deep trap states lies at the origin of the efficiency increase.

The antimony sulfide samples were further characterised by X-ray diffraction (XRD) measurements. The crystalline Sb_2S_3 samples were again annealed at 200 °C for different time periods in air. The measured XRD spectra are shown in Fig. 1c. While the spectra do not show peaks that can be attributed to antimony oxide, the relative height of the crystalline antimony sulfide peaks decreases with annealing time, indicating a decrease in crystallinity. Note that the crystallinity does not decrease continuously, but an abrupt reduction in the peak size is discernible between 1 min and 2 min.

Again, the composition of a sample that was heated at 200 °C in air for 15 hours was investigated. The XRD spectrum of this sample shows the almost complete loss in crystalline antimony sulfide and the appearance of different antimony oxide phases (Fig. S4, ESI†), indicating very strong oxidation.

To estimate the degree of surface oxidation of Sb_2S_3 films, X-ray photoemission spectroscopy measurements (XPS) were performed on films that were annealed for up to 20 min at T = 200 °C. The analysis of the O1s spectra is complicated by the position of the $Sb3d_{5/2}$ peak at 529.5 eV, closely overlapping with the O1s peak at 530.5 eV. For this reason, we analysed the $Sb3d_{3/2}$ peak, which appears at a much higher binding energy due to the relatively large spin–orbit splitting of Sb (9.35 eV).[20] As shown in Fig. 2a, this peak has two overlapping contributions, a peak at 538.5 eV assigned to Sb_2S_3 and a peak at 539.5 eV corresponding to antimony oxide (Sb_xO_y). The relative contributions are indicated in the figure. Fig. 2b shows the corresponding S2p spectra of Sb_2S_3 appearing at 160.9 eV and 162.05 eV, the relative heights of which are independent of annealing time. Their decrease in overall magnitude points to a decrease in Sb_2S_3 at the surface with increasing annealing time. The increase of the oxygen content with the annealing time was further confirmed by the O KL_1L_1 Auger peak in Fig. 2c.

Improved solar cell performance with antimony sulfide oxidation

To investigate the effect of surface oxidation on solar cell performance, photovoltaic devices were fabricated. A sintered layer of TiO_2 nano-crystals with an average diameter of 200 nm acted as a mesoporous n-type material and P3HT as a hole transport material. Electrons which are generated in the antimony sulfide sensitiser are injected into the TiO_2 anode and conducted towards the electrode by diffusion.[21] The highest occupied molecular orbital

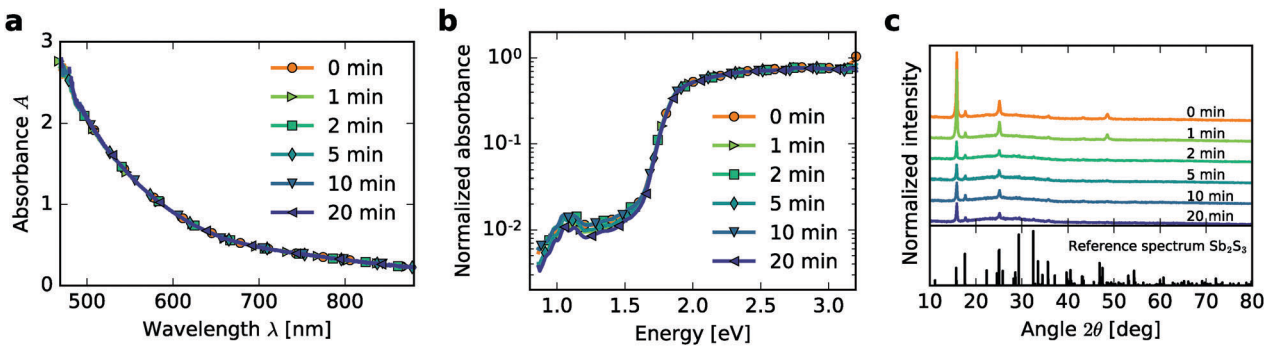

Fig. 1 (a) *In situ* absorbance measurements of antimony sulfide for six different oxidation times from 0 to 20 min at 200 °C. (b) Corresponding photothermal deflection spectroscopy (PDS) measurements. (c) Corresponding XRD spectra. The reference spectrum of crystalline Sb_2S_3 is shown at the bottom.[13]

 This journal is © the Owner Societies 2017

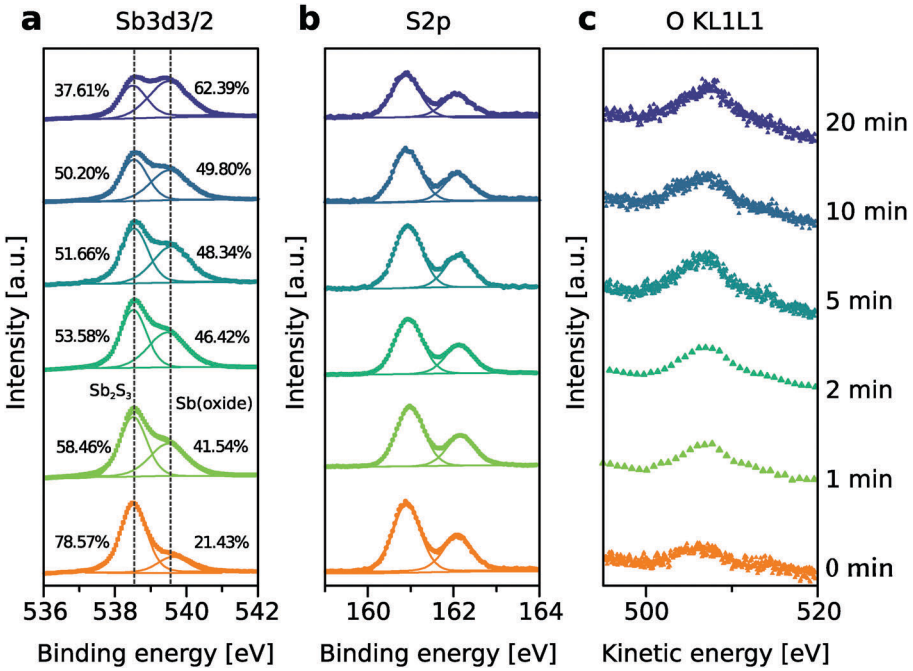

Fig. 2 X-ray photoemission spectroscopy (XPS) measurements of antimony sulfide films annealed up to 20 min at 200 °C in air. (a) The $Sb3d_{3/2}$ peak shows two contributions which can be assigned to antimony sulfide (538.5 eV) and antimony oxide (539.5 eV). (b) The S2p peaks decrease with increasing annealing time. (c) The O KL_1L_1 Auger peak increases with annealing time.

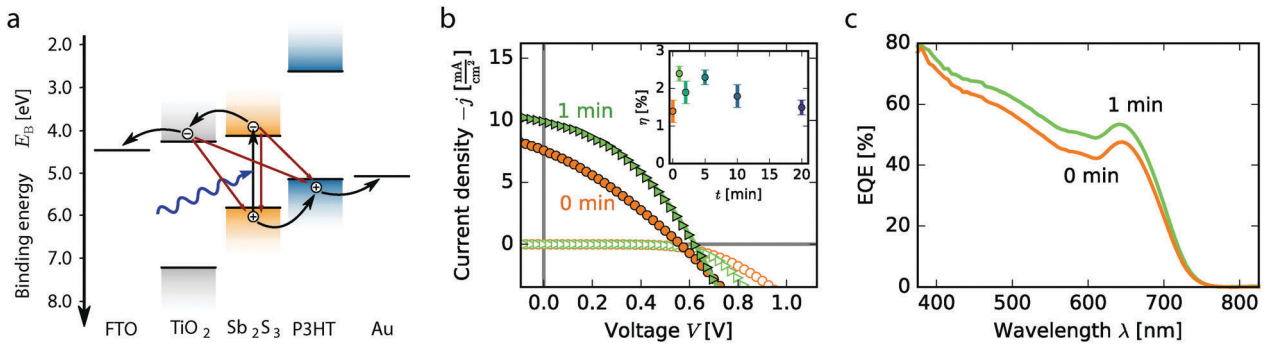

Fig. 3 (a) Simplified band diagram of the antimony sulfide sensitised solar cell fabricated in this study, with values for the energy levels from ref. 9. Loss mechanisms are indicated by red arrows showing four possible recombination pathways of charge carriers. (b) J–V characteristics of an unannealed and an annealed (1 min) solar cell under 1 Sun illumination (full symbols) and in the dark (open symbols). The inset shows the averaged efficiencies for different annealing times in air. (c) External quantum efficiencies of the same devices.

of the hole conductor P3HT lies above the valence band of Sb_2S_3 and thus allows the injection of holes into the P3HT layer. A schematic band diagram of the solar cell is shown in Fig. 3a.

Four different recombination pathways are also indicated in Fig. 3b. Electrons in the TiO_2 anode can recombine with holes in P3HT or holes in Sb_2S_3. Recombination can also take place in the absorber itself by direct recombination and holes in P3HT can recombine with negative charge carriers in the Sb_2S_3 layer.

For each annealing time (0–20 min), twelve solar cells were built and J–V curves were recorded. The photovoltaic parameters, including the short-circuit current density j_{sc}, open circuit voltage V_{oc}, fill factor and power conversion efficiency η, are summarised in Table 1 (see also Fig. S5, ESI†). The efficiency is also shown as a function of annealing time in the inset of Fig. 3b. It displays a broad maximum for t in the 1–5 min range followed by a gradual decrease.

Table 1 Photovoltaic parameters, including the power conversion efficiency η, short-circuit current density j_{sc}, open circuit voltage V_{oc} and fill factor FF, for five annealing times and unannealed samples. The listed values are averages from twelve solar cells each

[min]	η [%]	$-j_{sc}$ [mA cm^{-2}]	V_{oc} [mV]	[%]
0	1.4 ± 0.3	7.2 ± 0.9	566 ± 26	32.7 ± 4.5
1	2.4 ± 0.2	9.1 ± 0.5	619 ± 7	41.9 ± 2.0
2	1.9 ± 0.3	8.7 ± 0.8	599 ± 23	36.4 ± 2.9
5	2.3 ± 0.2	8.9 ± 0.5	608 ± 16	42.3 ± 2.4
10	1.8 ± 0.3	7.7 ± 0.8	609 ± 13	37.2 ± 3.0
20	1.5 ± 0.2	6.7 ± 0.9	590 ± 11	37.0 ± 1.7

Short annealing times greatly enhance the power conversion efficiency, from an average of η = 1.4% for 0 min to η = 2.4% for 1 min at 200 °C in air. Annealing times longer than 10 min have however a detrimental effect on device efficiencies. The performance increase arises from the combined improvement in j_{sc}, V_{oc} and FF. The performance decrease at long annealing times arises mostly from losses in the short circuit current, with V_{oc} and FF less affected.

Fig. 3b shows the *J–V* characteristics of an annealed device (1 min at 200 °C in air) and an unannealed solar cell. Current, voltage and the fill-factor are discernibly increased for the annealed sample. The increase in j_{sc} can also be appreciated from Fig. 3c, which shows the external quantum efficiency (EQE) of the two solar cells. The annealed sample shows higher EQE values across the entire visible spectrum. The dip at around λ = 600 nm is a well known feature arising from light absorption in P3HT.[22] Electrons generated in P3HT are inefficiently transported to the Sb_2S_3 layer.[22]

To ensure that the increase in the photovoltaic parameters is indeed due to surface oxidation and not caused by a different effect during the heat treatment, we undertook control measurements where the samples were heated at 200 °C for 1 min in air and in a nitrogen atmosphere. The samples that were annealed in a nitrogen atmosphere did not exhibit any improvement in device efficiency and their photovoltaic performance was inferior compared to the solar cells heated in air (Fig. S6, ESI†). This supports the hypothesis that surface oxidation lies at the origin of the efficiency enhancement.

Reduced recombination through oxidisation

High recombination rates lead to a decrease in the built-in potential.[23] A reduction of recombination should thus lead to a visible improvement of the open-circuit voltage V_{oc}. Further, high charge recombination also causes low fill factors.[24,25] Lower recombination rates should hence result in a clear enhancement of the fill factor. The effect of increased open-circuit voltage and the fill factor is indeed observed for the samples annealed in air, as shown in Fig. 3 and Fig. S5 (ESI†) and in Table 1. Reduced recombination also benefits the short-circuit current as it leads to an increased charge collection probability. This is reflected in the initial increase in j_{sc} for short annealing times (Fig. S5d, ESI†). On the other hand, very high oxidation levels complicate hole injection from the antimony sulfide absorber into P3HT, which leads to a reduction of the short-circuit current density and the fill factor for long annealing times (Table 1 and Fig. S5, ESI†).

To further probe the hypothesis that surface oxidisation during annealing in air leads to a reduction in the recombination rate, intensity modulated photocurrent spectroscopy (IMPS) and intensity modulated photovoltage spectroscopy (IMVS) measurements were performed. IMPS probes the photocurrent response of the solar cell under short-circuit conditions exposed to intensity modulated illumination. Equivalently, IMVS probes the photovoltage under open-circuit conditions.[21,26,27]

An array of three LEDs (λ = 625 nm) illuminated the device with different base irradiances and an additional sinusoidal variation with an amplitude of 10% of the base value was superposed. The measurement was undertaken as a function of the modulation frequency f of the light source and at different base level irradiances. The phase-shift of the response signal depends on the electron transport and on the electron recombination rate in IMPS and IMVS measurements, respectively.[21,26] The characteristic frequency f_c is the minimum of the imaginary part of the measured response. In IMPS measurements, the transport lifetime τ_{tr} of electrons is

$$\tau_{tr} = \frac{1}{2\pi f_c}. \quad (1)$$

The recombination lifetime τ_{rec} can likewise be determined from IMVS measurements. f_c is determined from the so-called Nyquist- and Bode-type plots for five base illumination values (Fig. S7, ESI†).

Fig. 4 shows the transport lifetimes and recombination lifetimes as a function of the short-circuit current and open-circuit voltage, based on eqn (1). The solid lines are a least-square single

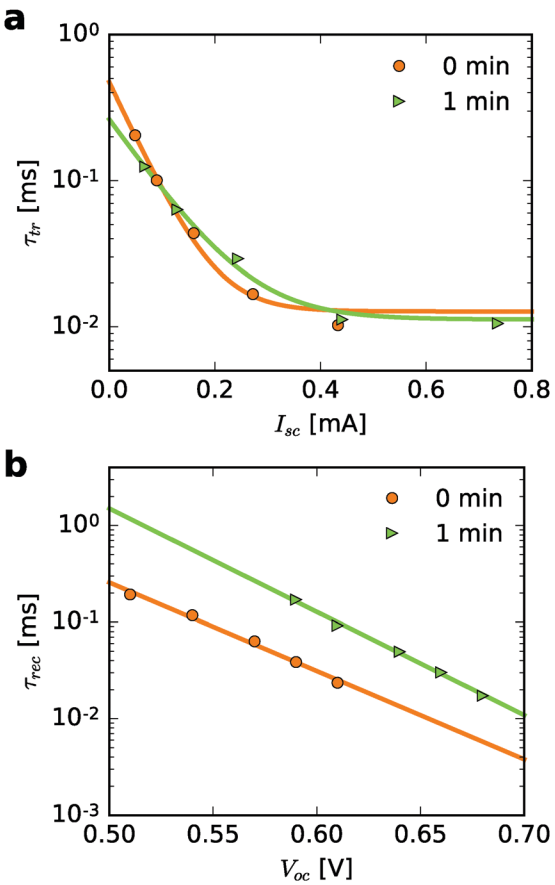

Fig. 4 (a) Electron transport times τ_{tr} determined by IMPS measurements of an unannealed (0 min) and an annealed (1 min at 200 °C in air) solar cell. (b) Electron recombination lifetimes τ_{rec} (from IMVS) for the same samples. The solid lines are single-exponential least-square fits. Annealing does not change the transport behaviour but reduces recombination by a factor of approximately four.

This journal is © the Owner Societies 2017

exponential fit of the form $\tau_{tr} = A_1 \exp(-B_1 \cdot I_{sc}) + C_1$ for IMPS and a logarithmic straight line $\ln(\tau_{rec}) = -A_2 \cdot V_{oc} + B_2$ for IMVS.[28] The fitting parameters and their standard deviations are listed in the ESI† (Table S1).

The transport lifetime τ_{tr} seems to be unaffected by the annealing procedure. Since the electron transport is dominated by diffusion in the mesoporous TiO_2 layer,[21] short annealing of the antimony sulfide-covered TiO_2 is not expected to alter the transport lifetime. Annealing the sample for 1 min at 200 °C in air does indeed increase the recombination lifetime of the charge carriers. Partial oxidisation of the absorber film decreases recombination at the antimony sulfide–P3HT interface, thereby improving the charge collection efficiency $\eta_{cc} = 1 - \frac{\tau_{tr}}{\tau_{rec}}$. As clearly visible in Fig. 4b, the recombination lifetime τ_{rec} of the annealed sample is higher by a factor of approximately four, compared to the unannealed sample. This observation again confirms the hypothesis that exposing antimony sulfide solar cells to high temperatures in air, which gives rise to a thin oxide layer, reduces charge carrier recombination and is hence beneficial for device performance. While similar passivation effects reducing charge carrier recombination can also be achieved by the deposition of a different material (*e.g.* ZnS[29] or SiO_2[30]), the presented annealing technique is facile, avoiding the additional processing involved in the deposition of additional layers.

Conclusion

This study shows the origin of a performance enhancing processing step of crystalline antimony sulfide used in solid state sensitised solar cells. Very brief heating of the samples in air at 200 °C leads to partial oxidisation of the antimony sulfide absorber film, which acts as a blocking layer for charge carriers, substantially reducing recombination at the Sb_2S_3–P3HT interface. The careful control of the level of oxidisation is however important since samples that were annealed for longer than 10 min show a deterioration in performance. Our conclusion is supported by an array of measurement techniques that demonstrate the controlled growth of an oxide surface layer (XPS) and the concomitant increase in the charge carrier recombination lifetime (IMVS), with all other structural and electronic parameters remaining unaffected. These results contribute to the ongoing quest for the performance enhancement in solution-processable all-inorganic sensitised solar cells, with the goal to provide a viable photovoltaic alternative with very long lifetimes.

Materials and methods

Preparation of photovoltaic cells

Fluorine doped tin oxide (FTO) coated glass slides (Solaronix, 15 Ω $\square^{-1}$) were coated with a thin (≈50 nm) compact TiO_2 blocking layer by spin-coating, as described elsewhere.[7] Dyesol paste (WER2-O) containing TiO_2 nanoparticles with an average size of 200 nm was diluted with anhydrous ethanol (2.5 ml EtOH per 1 g paste) and spin-cast onto the substrate at 1500 RPM for 45 s, resulting in an approximately 1.5 μm thick mesoporous TiO_2 scaffold. The substrates were sintered at T = 550 °C for 2 hours. After sintering, the mesoporous electrodes were soaked in an aqueous $TiCl_4$ bath (2×10^{-2} M) for 1 h at 70 °C. After rinsing with deionised water, the films were heated at 550 °C in air for 30 min and then allowed to cool to room temperature. Antimony sulfide was deposited using the chemical bath technique described by Messina *et al.*[11] The samples were submerged facing downwards into 100 ml of an aqueous solution containing 3.95 g $Na_2S_2O_3$ and 650 mg $SbCl_3$. The solution was kept at 10 °C for 1 h and then slowly cooled down to 6 °C in 1 h. After the deposition, the orange samples were rinsed in deionised water and dried with air. To turn Sb_2S_3 into its brown crystalline form, the films were heated at 250 °C for 45 min in a N_2 atmosphere. After this annealing step in a nitrogen-filled glove box, the samples were left to cool in the inert atmosphere.

For the experiments, the crystalline Sb_2S_3 samples were reheated to 200 °C in air for times varying from 0 to 20 min. P3HT (Merck lisicon) in chlorobenzene was deposited as a hole conducting material. In two subsequent steps P3HT was spin-coated onto the sample at 1500 RPM for 45 s, first, from a solution with a P3HT concentration of 5 mg ml^{-1}, followed by spin coating a solution with a 15 mg ml^{-1} P3HT concentration. Prior to spinning, the solution was spread across the substrate with the tip of a pipette and allowed to infiltrate the porous scaffold for 10 s. 100 nm thick gold electrodes were evaporated onto the samples using a Kurt J. Lesker e-beam evaporator. The active area of the solar cells in this study was 0.12 cm^2.

Material characterisation

Scanning electron microscopy was performed using a Zeiss LEO 1550 FE-SEM with a field emission source operating at 3 kV acceleration voltage. X-ray diffraction measurements were carried out using a Bruker D8 θ/θ (fixed sample) spectrometer with a position sensitive detector (LynxEye) and a standard detector (SC) with an auto-absorber and a graphite 2nd beam monochromator. The setup uses a Bragg Brentano parafocusing geometry and measures in the reflection mode. A single sample was used for XRD measurements. It was split into six parts prior to the annealing step. XPS samples were prepared on silicon wafers and were transferred into the ultra-high vacuum (UHV) chamber of an ESCALAB 250Xi. The measurements were carried out using a XR6 monochromated Alkα source (1486.6 eV) and a pass energy of 20 eV.

Optoelectronic characterisation

A solar simulator from ABET Technologies (Model 11016 Sun 2000) with a xenon arc lamp was used to illuminate the solar cells for *J*–*V*-measurements which were recorded using a Keithley 2635 sourcemeter. The intensity of the solar simulator is calibrated to 100 mW cm^{-2} using a silicon reference cell (Czibula & Grundmann FHG-ISE, RS-OD4). Prior to the measurement of the photovoltaic characteristics, the solar cells were light-soaked under the solar simulator for 15 min under open-circuit conditions.[31] The monochromatic light for the EQE-measurements came from a 250 W tungsten halogen lamp and an Oriel Cornerstone 130 monochromator. For IMPS and

IMVS, three LEDs (625 nm) driven by an Autolab LED Driver were used as a light source. The DC output of the Autolab LED Driver was controlled using the Autolab DAC164 and the AC output for the light modulation by the Autolab FRA32M module. The AC current amplitude was set to 10% of the DC current. The system was monitored and controlled *via* the software package NOVA (version 1.11). More information on the IMPS/IMVS analysis can be found in the ESI.†

Acknowledgements

K. C. G. thanks the Cambridge Trust, the Mott Fund for Physics of the Environment and Corpus Christi College Cambridge for funding. We thank Antonio Abate and Matt Menke for useful discussions. U.S. acknowledges funding from the Swiss National Science Foundation under Program NRP70 No. 153990.

References

1 B. O'Regan and M. Grätzel, *Nature*, 1991, **353**(6346), 737–740.
2 B. Li, L. Wang, B. Kang, P. Wang and Y. Qiu, *Sol. Energy Mater. Sol. Cells*, 2006, **90**(5), 549–573.
3 M. Y. Versavel and J. A. Haber, *Thin Solid Films*, 2007, **515**(18), 7171–7176.
4 S.-J. Moon, Y. Itzhaik, J.-H. Yum, S. M. Zakeeruddin, G. Hodes and M. Graetzel, *J. Phys. Chem. Lett.*, 2010, **1**(10), 1524–1527.
5 S. H. Im, C.-S. Lim, J. A. Chang, Y. H. Lee, N. Maiti, H.-J. Kim, M. K. Nazeeruddin, M. Grätzel and S. I. Seok, *Nano Lett.*, 2011, **11**(11), 4789–4793.
6 K. C. Gödel, Y. C. Choi, B. Roose, A. Sadhanala, H. J. Snaith, S. I. Seok, U. Steiner and S. K. Pathak, *Chem. Commun.*, 2015, **51**, 8640–8643.
7 Y. C. Choi, D. U. Lee, J. H. Noh, E. K. Kim and S. I. Seok, *Adv. Funct. Mater.*, 2014, **24**(23), 3587–3592.
8 Y. Itzhaik, O. Niitsoo, M. Page and G. Hodes, *J. Phys. Chem. C*, 2009, **113**, 4254–4256.
9 J. A. Chang, J. H. Rhee, S. H. Im, Y. H. Lee, H.-j. Kim, S. I. Seok, M. K. Nazeeruddin and M. Gratzel, *Nano Lett.*, 2010, **10**(7), 2609–2612.
10 M. T. S. Nair, Y. Pena, J. Campos, V. M. Garcia and P. K. Nair, *J. Electrochem. Soc.*, 1998, **145**(6), 2113–2120.
11 S. Messina, M. Nair and P. Nair, *Thin Solid Films*, 2007, **515**(15), 5777–5782.
12 N. Maiti, S. H. Im, C.-S. Lim and S. I. Seok, *Dalton Trans.*, 2012, **41**(38), 11569–11572.
13 A. Kyono and M. Kimata, *Am. Mineral.*, 2004, **89**, 932–940.
14 J. C. Cardoso, C. a. Grimes, X. Feng, X. Zhang, S. Komarneni, M. V. B. Zanoni and N. Bao, *Chem. Commun.*, 2012, **48**(22), 2818–2820.
15 S. Ito, K. Tsujimoto, D.-C. Nguyen, K. Manabe and H. Nishino, *Int. J. Hydrogen Energy*, 2013, **38**(26), 16749–16754.
16 A. Nikolakopoulou, D. Raptis, V. Dracopoulos, L. Sygellou, K. S. Andrikopoulos and P. Lianos, *J. Power Sources*, 2015, **278**, 404–410.
17 D. Raptis, G. Sfyri, L. Sygellou, V. Dracopoulos, E. Nouri and P. Lianos, *RSC Adv.*, 2016, **6**, 49537–49542.
18 W. B. Jackson, N. M. Amer, A. C. Boccara and D. Fournier, *Appl. Opt.*, 1981, **20**(8), 1333.
19 A. Sadhanala, F. Deschler, T. H. Thomas, S. E. Dutton, K. C. Goedel, F. C. Hanusch, M. L. Lai, U. Steiner, T. Bein and P. Docampo, *et al.*, *J. Phys. Chem. Lett.*, 2014, **5**(15), 2501–2505.
20 T. Birchall, J. Connor and L. Hillier, *J. Chem. Soc., Dalton Trans.*, 1975, 1973–1976.
21 L. Dloczik, O. Ileperuma, I. Lauermann, L. M. Peter, E. A. Ponomarev, G. Redmond, N. J. Shaw and I. Uhlendorf, *J. Phys. Chem. B*, 1997, **101**(49), 10281–10289.
22 J. A. Chang, S. H. Im, Y. H. Lee, H.-J. Kim, C.-S. Lim, J. H. Heo and S. I. Seok, *Nano Lett.*, 2012, **12**(4), 1863–1867.
23 P. P. Boix, G. Larramona, A. Jacob, B. Delatouche, I. Mora-Seró and J. Bisquert, *J. Phys. Chem. C*, 2012, **116**, 1579–1587.
24 E. Palomares, J. N. Clifford, S. A. Haque, T. Lutz and J. R. Durrant, *Chem. Commun.*, 2002, (14), 1464–1465.
25 D. Bartesaghi, I. del Carmen Pérez, J. Kniepert, S. Roland, M. Turbiez, D. Neher and L. J. A. Koster, *Nat. Commun.*, 2015, **6**, 7083.
26 G. Schlichthörl, S. Y. Huang, J. Sprague and A. J. Frank, *J. Phys. Chem. B*, 1997, **101**(41), 8141–8155.
27 P. R. F. Barnes, K. Miettunen, X. Li, A. Y. Anderson, T. Bessho, M. Gratzel and B. C. O'Regan, *Adv. Mater.*, 2013, **25**(13), 1881–1922.
28 B. Roose, K. C. Gödel, S. Pathak, A. Sadhanala, J. P. C. Baena, B. D. Wilts, H. J. Snaith, U. Wiesner, M. Grätzel, U. Steiner and A. Abate, *Adv. Energy Mater.*, 2016, **6**(2), 1501868.
29 I. Mora-Seró, S. Giménez, F. Fabregat-Santiago, R. Gómez, Q. Shen, T. Toyoda and J. Bisquert, *Acc. Chem. Res.*, 2009, **42**(11), 1848–1857.
30 Z. Liu, M. Miyauchi, Y. Uemura, Y. Cui, K. Hara, Z. Zhao, K. Sunahara and A. Furube, *Appl. Phys. Lett.*, 2010, **96**(23), 233107.
31 S. Nezu, G. Larramona, C. Choné, A. Jacob, B. Delatouche, D. Peŕé and C. Moisan, *J. Phys. Chem. C*, 2010, **114**(14), 6854–6859.

 This journal is © the Owner Societies 2017